Enhanced phonon scattering in staggered-pore silicon metamaterials: a non-equilibrium molecular dynamics study

***Othman* Soubai[1*], *Younes* Abouelhanoune[1], and *Mohammed* Taibi[1]**

[1]Abdelmalek Essaadi University, ENSAH, LSA Laboratory, Al-Hoceima, Morocco.

Abstract. Porous silicon nanostructures are promising candidates for thermal management applications, but the relationship between pore architecture and thermal transport remains incompletely understood. Here we use non-equilibrium molecular dynamics (NEMD) simulations with the Müller-Plathe method and the Stillinger–Weber potential to investigate how a staggered zigzag pore-wall architecture influences phonon heat transport in silicon at 300 K. Three structures are compared at matched system size: bulk silicon ($\varphi = 0\%$), a single-pore geometry ($\varphi = 6.84\%$), and a staggered zigzag configuration with two offset cubic pores ($\varphi = 28.27\%$). A size-scaling study on bulk silicon confirms that the simulations operate in the ballistic transport regime and extrapolate to the experimental bulk thermal conductivity of 148 W/(m·K). At the matched comparison size of 26.1 nm, the porous structures achieve thermal conductivity reductions of 37% and 78% relative to bulk silicon. The porosity dependence follows a power law $\kappa = \kappa_0(1 - \varphi)^n$ with $n \approx 4.70$, exceeding the effective medium theory exponent ($n = 1.5$) by a factor of 3.1. These findings demonstrate that pore architecture can be a more effective design lever than porosity fraction alone for thermal conductivity reduction.

Keywords: thermal conductivity, porous silicon, molecular dynamics, phonon scattering, thermal metamaterials.

1 Introduction

Thermal management has been recognized to be one of the major barriers for advanced semiconductor technologies, where increasing power density requires the development of materials with engineered thermal transport properties [1,2]. Nanoporous silicon has been recognized to be of particular interest for its tunable thermal conductivity, covering a wide range from close to its bulk value of 148 W/(m·K) to close to its amorphous limit, depending on the size, shape, and spatial distribution of its internal voids [3–5]. The maturity of silicon technology and its established fabrication routes make it a promising candidate for the development of thermal metamaterials.

---

* *Corresponding author: othman.soubai@etu.uae.ac.ma*

Previous atomistic simulations revealed that the introduction of porosity into silicon materials can decrease its thermal conductivity by one or two orders of magnitude [3,6]. By employing molecular and lattice dynamics, He et al. [4] found that the decrease in thermal conductivity is caused by the appearance of non-propagating diffusive modes and a decrease in the group velocities of the propagating modes.

Fang and Pilon [7] employed equilibrium molecular dynamics simulations and found scaling laws relating κ, porosity, pore size, and interpore spacing. Recently, de Sousa Oliveira and Neophytou [8] investigated more than 50 geometries of nanoporous silicon materials with different pore geometries and found that the "line-of-sight" blocking effect is more important than porosity or surface-to-volume ratio in controlling κ values. Following this line, de Sousa Oliveira and co-workers [9] found that there is a heat current anticorrelation in specific geometries, where specular reflections can enhance κ reductions by up to 80% above those expected from porosity. Hosseini et al. [10] also showed that the super-suppression selectively suppresses long-wavelength, long MFP phonons that dominate heat conduction, and Greaney et al. [11] verified the phenomenon by using the non-equilibrium Green's function and Monte Carlo simulations.

Line-of-sight blocking can also be naturally extended to a broader thermal metamaterials framework, in which heat transport can be controlled and hindered by geometric design, not just by chemistry alone [1]. Using Boltzmann transport calculations, Romano and Grossman [12,13] demonstrated that for disordered nanoporous materials, it is not just the density of pores but their arrangement that can significantly affect heat transport and that the "phonon bottleneck" — the smallest distance between pores — can be a critical dimension. Experiments by Hopkins et al. [6] and Yu et al. [5] showed that periodic pore patterning in silicon thin films can reduce thermal conductivity κ by over an order of magnitude compared to bulk silicon, compatible with strong boundary scattering at pore surfaces. Yang et al. [14] have extended these concepts to 3D silicon phononic crystals with spherical voids, where thermal conductivity κ reductions of up to 300 times can be achieved at 50% porosity, along with increasing phonon localization for higher porosity levels. In a similar vein, de Araujo Oliveira et al. [15] have demonstrated that κ in silicon phononic crystals is ultimately limited by the neck size (the minimum distance between neighboring defects).

Despite this progress, most computational studies of porous silicon have employed either randomly distributed pores or simple periodic arrays of aligned cylindrical channels. Recent NEMD studies have begun exploring more complex configurations — for example, Hahn et al. [16] investigated step-like and random pore distributions in nanoporous silicon membranes and found that the pore arrangement significantly affects both the thermal conductivity and the thermal rectification behavior — but the thermal transport consequences of deliberately engineered, non-trivial pore architectures where pore placement is optimized to maximize phonon path tortuosity remain relatively unexplored. In particular, the question of whether architecture effects can be quantified through a simple structure–property relationship, and whether such effects can be cleanly separated from finite-size artifacts, has not been systematically addressed.

In this work, we investigate a staggered zigzag pore-wall architecture in which two offset cubic pores force heat-carrying phonons through narrow wall channels with multiple directional changes. Using non-equilibrium molecular dynamics (NEMD) simulations with the Müller-Plathe reverse perturbation method [17], we characterize three silicon structures — bulk, single-pore, and staggered zigzag — at matched system size. A four-point size-scaling study on bulk silicon validates the methodology against the known experimental thermal conductivity. We quantify the architecture enhancement through a power law analysis and compare the resulting exponent with effective medium theory predictions. Section 2 describes the computational methods, including the pore geometry design and NEMD protocol. Section 3 presents the results, beginning with size-scaling validation, followed by the porosity study and a discussion of the phonon scattering mechanism. Section 4 concludes the manuscript.

2 Computational methods

2.1 Interatomic potential and crystal structure

All molecular-dynamics simulations were carried out with LAMMPS [18]. Interactions between Si atoms were described using the Stillinger–Weber (SW) potential [19], which includes both two-body and three-body terms required to reproduce the tetrahedral bonding of diamond-cubic silicon. The SW potential has been widely benchmarked for silicon thermal-transport calculations and is commonly used in phonon-mediated heat-conduction studies [20,21].

Simulation supercells were built from the diamond-cubic Si unit cell (lattice constant a = 5.431 Å, 8 atoms per unit cell). The cross-section was fixed at 8 × 8 unit cells in x and y (43.45 Å × 43.45 Å), corresponding to a cross-sectional area A = 1888 Å^2 normal to the heat-flow direction. The length along the transport direction (z) was systematically varied as described in Section 2.3. Periodic boundary conditions were applied in x, y, and z. In the porous models, periodic boundary conditions generate pores that repeat indefinitely in all three spatial directions, so the system represents a phononic crystal rather than a single isolated pore. In the direction of heat conduction (z-direction), such periodicity ensures that the phonons escaping from one unit cell will be immediately entering the next unit cell, and therefore the thermal conductivity κ calculated would refer to heat conduction through periodic pore structure. Periodicity along the other two directions (x- and y-directions) would result in uniform pore structure and eliminate effects due to disorder in the plane of the pores. As all three systems were simulated under same periodic boundary conditions with equal sized systems, artifacts from periodic boundaries can be considered equal among the three.

2.2 Porous structure design

Three materials were studied: bulk silicon and two nanoporous structures with varying degrees of porosity. The formation of pores was done by removing atoms in pre-defined blocks utilizing the LAMMPS region and delete_atoms commands. Since LAMMPS removes atoms at the boundary of the specified region, the actual porosities obtained are somewhat higher than the geometrical porosities; the number of atoms and porosities used below are directly obtained from LAMMPS output.

At N_z = 48 (8 × 8 × 48 unit cells), the pristine reference system contains 24,576 atoms.

Low-porosity structure (φ = 6.84%): We removed a single cubic void spanning lattice units [1,4] in both x and z, leaving 22,896 atoms. This simple geometry forces phonons to detour around one obstacle while preserving relatively direct pathways elsewhere.

High-porosity structure (φ = 28.27%): Two cubic pores were placed in an offset, staggered "zigzag" arrangement—Pore A in the lower-left quadrant (lattice units [0,4] × [0,4] in x–z) and Pore B in the upper-right quadrant (lattice units [4,8] × [4,8] in x–z). This layout creates narrow solid necks around the pores, as well as forcing the heat-carrying phonons to travel through the tortuous channels in the walls of the structure, which have directional turns to enhance boundary scattering, as opposed to material removal. The structure contains 17,629 atoms.

The exact geometric parameters used to define the pore regions are listed in Table 1b. All coordinates are given in lattice units (1 l.u. = 5.431 Å). The smallest solid neck separating Pore A and Pore B measures 4 lattice units (≈21.7 Å ≈ 2.2 nm) in both *x* and *z* directions, which is well below the dominant phonon mean free path in silicon at 300 K (~300 nm). These specifications provide enough detail for another researcher to reproduce the structures using the LAMMPS region and delete_atoms commands.

Table 1. Structural parameters of the simulated silicon systems for $N_z = 48$.

Structure	Designed φ (%)	Actual φ (%)	Atoms	Pore geometry
Bulk Si	0	0	24,576	None
Porous (low)	5.27	6.84	22,896	Single cubic pore
Porous (high)	25.0	28.27	17,629	Staggered zigzag

Table 1b. Pore region coordinates in lattice units (1 l.u. = 5.431 Å = *a*). Heat flows along *z*.

Pore	x range (l.u.)	y range (l.u.)	z range (l.u.)	Neck width (l.u.)
Low: single pore	[1, 4]	[0, 8]	[1, 4]	4
High: Pore A	[0, 4]	[0, 8]	[0, 4]	—
High: Pore B	[4, 8]	[0, 8]	[4, 8]	4 (A–B gap)

2.3 Non-equilibrium molecular dynamics (NEMD)

Thermal conductivity was computed using the reverse non-equilibrium molecular dynamics (rNEMD) method of Müller-Plathe [17]. In this approach, an artificial heat flux is imposed by periodically exchanging the velocity vectors of the hottest atom in the cold slab (at $z = 0$) with the coldest atom in the hot slab (at $z = L_z/2$). The resulting steady-state temperature gradient is then used to extract the thermal conductivity via Fourier's law:

$$\kappa = \frac{\Sigma \Delta E_{\mathrm{swap}}}{2\, t_{\mathrm{prod}}\, A\, |dT/dz|} \qquad (1)$$

where $\Sigma\Delta E_{\mathrm{swap}}$ is the total kinetic energy transferred during production, t_{prod} is the production time, *A* is the cross-sectional area perpendicular to the heat flow, and $\mathrm{d}T/\mathrm{d}z$ is the steady-state temperature gradient. The factor of 2 accounts for the two symmetric heat flow paths in the periodic simulation cell.

The NEMD method was chosen over the equilibrium Green–Kubo (GK) approach for two reasons. First, preliminary GK calculations on porous structures showed poor convergence of the heat flux autocorrelation function at the accessible system sizes. Second, NEMD has the merit of directly investigating the heat flow through the pore structure, such that the relationship between the temperature profile and the underlying scattering physics is easier to interpret. For systems of such size in the nanostructure and porous regime, NEMD is commonly employed to calculate the value of κ as mentioned in references [3,4].

For the purpose of binning the temperatures, the cell was divided into 20 equal slabs in the *z*-direction. This resulted in the number of atoms per slab being in the order of ~600, even in the highest porosity case, such that the statistics for the time-average of the temperatures can be stably computed. Velocity exchanges were performed every 100 timesteps.

2.4 Size-scaling protocol

Finite-size effects are one of the major limitations in the prediction of thermal conductivity κ by MD methods [19,21]. When the simulation length L_z is smaller than the average phonon mean free path, phonons will experience more scattering with periodic boundaries than from their intrinsic anharmonicity, resulting in $\kappa < \kappa_{\text{bulk}}$. The MFP of phonons in silicon at 300 K has been reported to be of order ~300 nm [22], which is much larger than the domain sizes we can access in MD simulation.

To assess and correct these finite-size trends, we ran a bulk-Si size-scaling series with N_z = 24, 48, 96, and 192 (L_z = 13.0–104.3 nm; 12,288–98,304 atoms; Table 2). In the ballistic regime, the size dependence of κ follows [19]:

$$\frac{1}{\kappa(L_z)} = \frac{1}{\kappa_\infty} + \frac{C}{L_z} \tag{2}$$

where κ_∞ is the bulk (infinite-size) thermal conductivity and *C* is a constant related to the phonon MFP distribution. A linear fit to 1/κ versus $1/L_z$ allows extrapolation to the infinite-size limit.

For the porosity comparison, bulk, low-porosity, and high-porosity systems were all simulated at the same size (N_z = 48; L_z = 26.1 nm) so that finite-size effects largely cancel in relative comparisons.

2.5 Simulation protocol and statistical averaging

Each run followed a three-step process. (i) The structure was energy-minimized using a conjugate gradient algorithm. (ii) Equilibration was carried out in the NVT ensemble at 300 K for 100 ps using a Nosé–Hoover thermostat with a coupling constant of 0.1 ps. (iii) The thermostat was removed and the system was evolved in NVE for 500 ps with velocity swaps to create the steady-state temperature gradient.

We employed a 1 fs timestep. Temperature profiles were saved every 10 ps (50 snapshots over the production phase). To enhance statistical accuracy, each structure was simulated with three different initial velocity seeds (12345, 34567, 56789). The values of κ and the temperature profiles provided here are the average of the three seeds, computed over the last 80% of the run time to avoid the initial transients; the uncertainties given are the standard deviation of the seeds.

The SW potential has been recognized to have a small tendency to underestimate silicon's thermal conductivity in comparison to first-principles approaches [22]. However, since we discuss relative reductions and architecture-driven trends and not absolute κ, this effect does not alter the overall results. The calculations have been performed on the MARWAN HPC cluster, utilizing 16 MPI ranks for each simulation.

3 Results and discussion

3.1 Size-scaling analysis and methodology validation

To confirm the NEMD setup, we performed a size-scaling simulation on bulk Si. In Fig. 3(a), $1/\kappa$ is plotted versus $1/L_z$ for four lengths (L_z = 13.0–104.3 nm; 12,288–98,304 atoms). The linear trend, expected for boxes shorter than the dominant phonon MFP, is evident. In this ballistic transport regime, κ varies approximately linearly with L_z, since many phonons pass through the simulation cell with limited intrinsic Umklapp scattering. The linearity of the $1/\kappa$ vs. $1/L_z$ plot in Fig. 3(a) confirms that the four data points are mutually consistent and that no anomalous scattering artifacts contaminate the results at any of the four system sizes.

Table 2 and Figure 3(b) summarize the measured κ values, which rise from 6.0 ± 0.5 W/(m·K) at L_z = 13.0 nm to 52.1 ± 5.7 W/(m·K) at L_z = 104.3 nm. Extrapolating the linear $1/\kappa$ versus $1/L_z$ trend to $1/L_z \rightarrow 0$ yields $\kappa_\infty \approx 148$ W/(m·K), consistent with the accepted experimental value at 300 K [23] and prior SW-based MD results [19,20,21]. All simulations considered in this work fall within the ballistic transport regime, since the system length in the z direction L_z is far smaller than the phonon mean free path in silicon (~ 300 nm). Under these conditions, the computed thermal conductivity values are lowered by finite-size effects and therefore should not be interpreted as bulk diffusive-limit properties. Even so, comparisons among structures with the same L_z remain meaningful because each system is affected by the same degree of finite-size suppression. Consequently, the EMT analysis in Section 3.4 compares the reduction caused by the pore architecture at L_z =26.1 nm with the porosity-based reduction predicted by EMT for the same porosity level, yielding a ratio that is expected to be only weakly dependent on the transport regime.

Table 2. NEMD thermal conductivity of bulk silicon as a function of system size. Uncertainties represent the standard deviation over three independent seeds.

N_z	L_z (nm)	Atoms	κ (W/(m·K))
24	13.03	12,288	6.02 ± 0.48
48	26.07	24,576	12.03 ± 0.29
96	52.14	49,152	27.93 ± 3.17
192	104.28	98,304	52.05 ± 5.73

3.2 Phonon transport pathways in porous architectures

The progressive constraining of the phonon transport pathways is demonstrated in Figure 1. For the bulk structure (Figure 1(a)), the phonons travel along unimpeded direct paths between the cold and hot slabs. The uniform atom distribution visible in the cross-section confirms the defect-free diamond cubic lattice used as the baseline. The addition of a single cube-shaped pore (Figure 1(b)) causes the phonons to curve around the pore, lengthening the travel distance and causing additional scattering at the pore boundaries. Crucially, the unimpeded straight-line travel paths through the material remain above and below the pore, as indicated by the continuous solid region at x > 21.7 Å in Figure 1(b).

The staggered zigzag configuration (Figure 1(c)) completely eliminates this possibility. The offsetting of the two pores eliminates all direct paths in the direction of heat flow. Phonons entering from the cold slab must travel upward in the wall channel above Pore A, pass through the bottleneck boundary between the two pore regions, and then travel downward in the channel below Pore B before reaching the hot slab. The yellow shading in Figure 1(c) indicates the narrow wall channels, which are less than 2.2 nm in width, much less than the dominant mean free path of phonons in silicon at 300 K, which acts as strong bottlenecks for the phonons. The zigzag configuration requires the phonon to make two abrupt changes in direction, resulting in additional boundary-driven scatterings. To highlight the importance of the offset placement, we note that if Pores A and B were aligned (i.e., both placed in the same quadrant), phonons could pass through the solid region adjacent to both pores without any directional change. The staggered configuration is specifically designed to eliminate all such direct corridors, which is the essential distinction from conventional aligned-pore architectures studied in previous work [3,7,8].

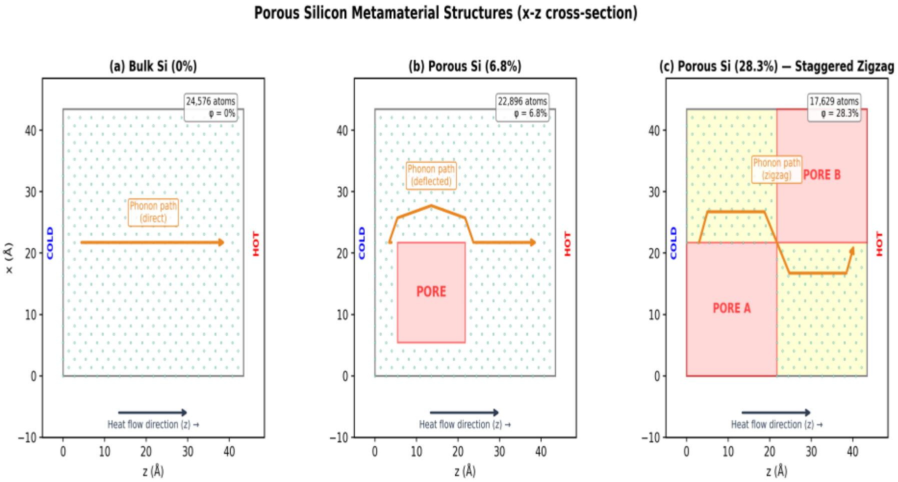

Fig. 1. Atomic structure schematics (*x*–*z* cross-sections) for (a) bulk Si (24,576 atoms, φ = 0%), (b) low-porosity Si (22,896 atoms, φ = 6.84%) with a single cubic pore, and (c) high-porosity Si (17,629 atoms, φ = 28.27%) with a staggered, offset-pore ("zigzag") architecture. Orange arrows sketch representative phonon transport routes. Yellow shading in (c) highlights the constricted solid necks between offset pores.

3.3 Temperature profiles and heat transport

The summary of steady-state temperature distributions achieved during the NEMD simulations is presented in Figure 2 below. As illustrated by the upper images of Figure 2 where heat map representations of the structures with a common color bar (283 – 325 K) are used, while the temperature distribution in the bulk structure (Fig. 2, left) appears rather homogeneous, i.e., dominated by light blue, a significant variation is seen for the structure with a high porosity (Fig. 2, right), which is represented by a clear change in colors from blue to red due to a higher temperature decrease.

Figure 2's lower plot shows the temperature distribution in the z-direction across the three independent random seeds used for the final 80% of the 500 ps production cycle. For bulk Si, the half-cell temperature drop is $\Delta T = 8.7$ K, signifying its effective thermal conductivity properties. On the other hand, for the staggered high porosity configuration, the temperature drop is $\Delta T = 39.7$ K, which is about 4.6 times greater. This implies a notable interference with phonon transport. The low porosity configuration falls somewhere between, with a ΔT of 14.3 K.

The gradual increase in the slope from bulk, nonporous to porous is clear proof of increased phonon scattering as pores are added. In the case of equal heat flow in the simulation runs, an increase in ΔT leads to a decrease in the thermal conductivity κ using Fourier's law. The range of variation within the seed configurations (shaded areas in Figure 2) is quite small relative to the difference between the configurations, proving their statistical significance. More importantly, in the case of the porous configuration, the ranges are hardly distinguishable, implying very low interseed variability (less than 1% standard deviation). This is because the zigzag channels force the phonons to follow a single path.

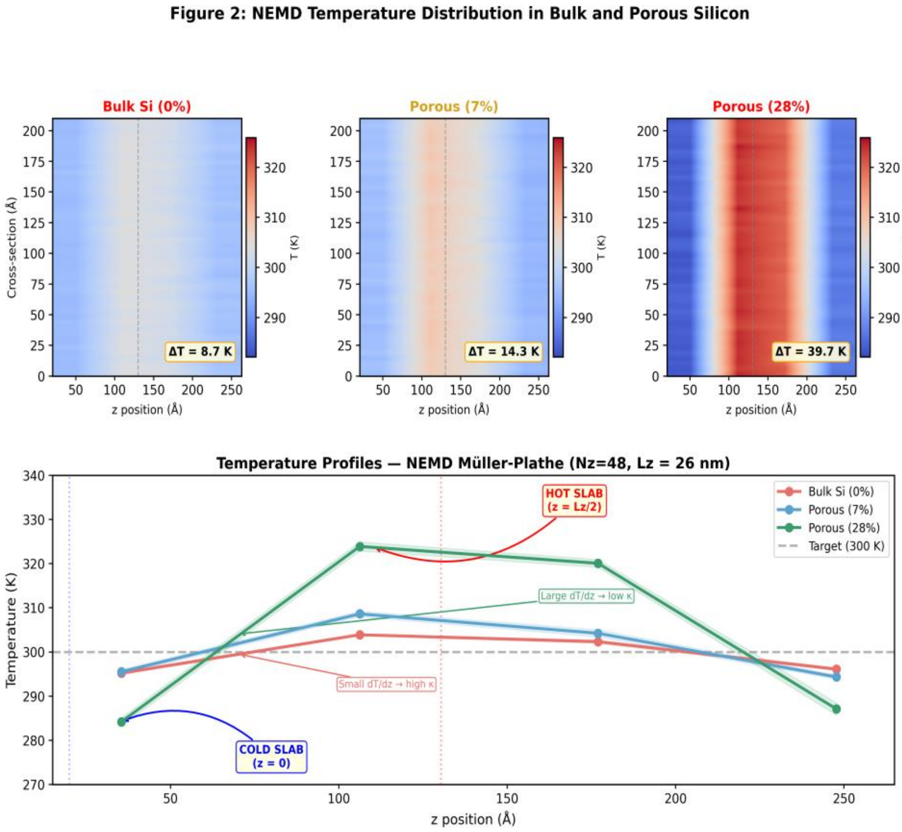

Fig. 2. NEMD temperature distributions for bulk and porous silicon at $N_z = 48$ ($L_z = 26.1$ nm). Top row: temperature heat maps with consistent colorbar. Bottom: overlaid temperature profiles averaged over three independent seeds; shaded bands show seed-to-seed variability.

3.4 Porosity-dependent thermal conductivity and power law analysis

The thermal conductivities of all three structures for the matched system size of $N_z = 48$, or $L_z = 26.1$ nm, are compared in Figure 3(c) and listed in Table 3. The reference value for bulk silicon is κ = 12.03 ± 0.29 W/(m·K) for this system size. As shown in Fig. 3(c), the bar heights decrease monotonically with increasing porosity, and the error bars confirm that the three structures are statistically well separated. Introducing 6.84% porosity with a single-pore structure decreases the thermal conductivity to 7.63 ± 0.99 W/(m·K), a reduction of 37%

relative to the bulk. The staggered zigzag structure with porosity of 28.27% results in $\kappa = 2.59 \pm 0.02$ W/(m·K), a reduction of 78%.

Table 3. NEMD thermal conductivity of bulk and porous silicon at $N_z = 48$ ($L_z = 26.1$ nm).

Structure	**φ (%)**	**Atoms**	**κ (W/(m·K))**	**ΔT (K)**	**Red. (%)**
Bulk Si	0	24,576	12.03 ± 0.29	8.7	—
Porous (low)	6.84	22,896	7.63 ± 0.99	14.3	37
Porous (high)	28.27	17,629	2.59 ± 0.02	39.7	78

The 78% reduction at only 28% porosity is an extremely high value. For comparison, if 28% of the material is removed from a homogeneous medium, the reduction in thermal conductivity would typically be around 35–40% according to standard effective medium theory (EMT) models, such as the Maxwell–Garnett or Bruggeman equations [24]. The actual reduction is approximately two times larger than the EMT prediction.

To parameterize the porosity dependence, we fit the value of κ to a power law form $\kappa = \kappa_0(1 - \varphi)^n$, with κ_0 being the value of κ at zero porosity (12.03 W/(m·K) for $L_z = 26.1$ nm), φ the porosity fraction, and *n* an effective exponent. Based on two non-zero porosity data points, we have n = 4.70, 3.1 times higher than the EMT estimate of n = 1.5. This exponent was obtained using just two porosities, 6.84% and 28.27%, which is enough for determining a single power-law exponent but not for validating its form or quantifying the uncertainty in n. For n = 4.70, the reader should keep in mind that this number is more of a reflection of the magnitude of enhancement due to the structure than an exact constant for the material. More simulations with different porosities (10%, 15%, 20%, etc.) are anticipated but not required for concluding that there is a power-law scaling and obtaining an accurate exponent. But the key conclusion about the staggered zigzag lattice providing an enormous enhancement in phonon scattering compared to the effect of porosity alone is valid no matter the specific exponent value.

The enhancement may be understood via the phonon route scheme provided in Section 3.2. For the staggered structure, the direct hot-to-cold phonon paths are blocked, causing phonons to travel through the ~2.2 nm wall channels, which function as phonon bottlenecks. Geometrical confinement in the channels, along with the forced turns at the pore boundary, creates a compound phonon scattering event, resulting in the reduction of κ beyond the EMT "removed material" prediction. This view is also supported by the observation that sub-MFP features, particularly in nanostructured silicon, increase boundary scattering and phonon filtering [12,25], as well as the heat current anticorrelation mechanism for closely spaced pores, as suggested by de Sousa Oliveira et al. [9] and Hosseini et al. [10]. In Fig. 3(d), the power-law fitting curve (blue dashed) shows a steeper slope than the EMT benchmark (gray dotted) due to the staggered design, which indicates a scaling up of the porosity influence by a quantity increasing as φ increases. This trend is evident even for low values of φ, around 7%, while at 28%, there is a huge difference in κ from the EMT benchmark.

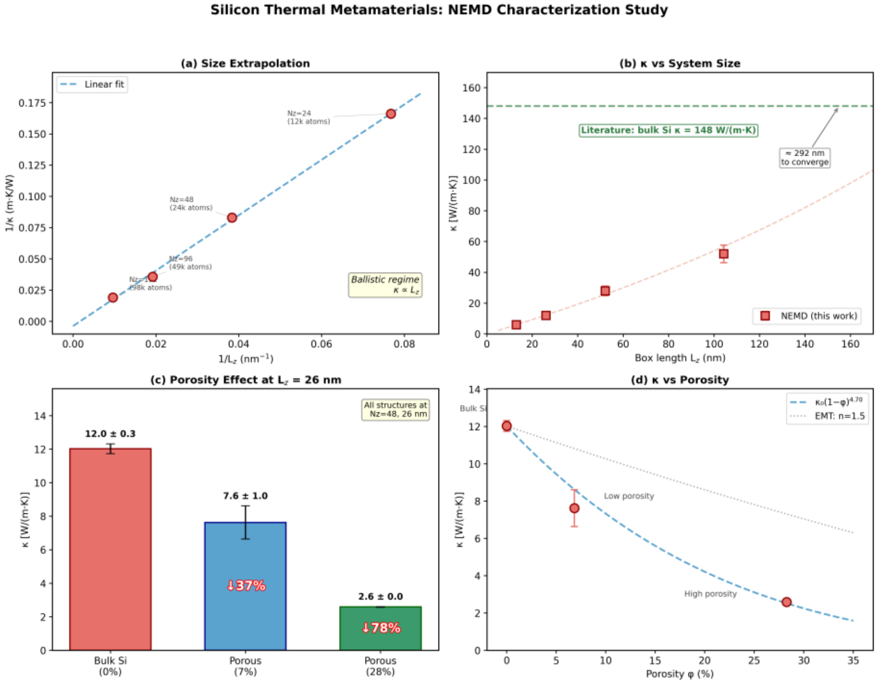

Fig. 3. NEMD thermal-conductivity characterization for bulk and porous silicon. (a) $1/\kappa$ versus $1/L_z$ for bulk Si. (b) κ versus L_z. (c) κ for bulk, low-porosity ($\varphi = 6.84\%$), and high-porosity ($\varphi = 28.27\%$) structures at matched size. (d) κ versus porosity with power-law fit ($n = 4.70$) compared with EMT reference ($n = 1.5$). Error bars denote standard deviation over three independent seeds.

3.5 Comparison with previous work

These results are then put into perspective in relation to previous theoretical and experimental work on the thermal properties of nanoporous-Si material. In the previous theoretical research, the percentage of reduction in thermal conductivity of nanoporous Si has ranged from 50–90% [3,4,8]. This percentage reduction falls in line with the results reported here with a 78% reduction at 28.27% porosity.

One-on-one numeric comparison needs to be done with caution since previous researches may vary significantly from each other due to different interatomic potentials, methodology, size limitations of available systems, and pore geometries. An interesting parameter for comparison is the exponent n in $\kappa(\varphi) = \kappa 0(1 - \varphi)n$. EMT predicts $n = 1.5$ for spherical pores [24]. In the case of aligned cylinders, MD calculations show that n is between 1.5 and 2.5 [3,7], while in the case of disordered configurations, which have higher line-of-sight blockage, the value of n varies between 2 and 3 [4,8,26]. For staggered zigzag configuration, we observe $n = 4.70$, a value which is much higher than the above-mentioned intervals. Since aligned and disordered configurations show $n \leq 3$ at approximately the same porosity fraction, while $n = 4.70$ in our staggered zigzag case, it means that such high reduction is due to the designed zigzag configuration.

Table 4. Comparison with selected computational studies of porous silicon thermal conductivity.

Study	Method	Pore type	Porosity	n	Key finding
Lee et al. [3]	EMD	Cyl., aligned	7–38%	~2.0	First MD nanoporous Si
He et al. [4]	EMD+LD	Cyl., disord.	13–35%	~2.5	Disorder compounds
Fang & Pilon [7]	EMD	Spherical	10–40%	~1.8	Scaling laws
Dettori et al. [26]	EMD	Cyl./voids	5–30%	~2.0	Interface density
de Sousa Oliveira [8]	EMD	50+ geom.	5–40%	2–3	Line-of-sight
de Sousa Oliveira [9]	EMD	Closely spaced	3–15%	—	Anticorrelation
Hosseini et al. [10]	EMD+MC	Constricted	3–15%	—	Super-suppression
Hahn et al. [16]	NEMD	Step-like	2–10%	—	Rectification
de Araujo Oliveira [15]	HNEMD	Defect motifs	10–40%	—	Neck size limits κ
This work	**NEMD**	**Staggered zigzag**	**0–28%**	**4.70**	**Architecture >> φ**

Experimentally, Gesele et al. [27] found κ ranging from 0.05 to 0.8 W/(m·K) at 300 K for mesoporous silicon with porosities between 64% and 89%. Zhu et al. [28] also found significant anisotropy in porous silicon membranes. While it is difficult to make a direct comparison due to the differing porosity ranges and surface oxidation of the real samples, the results from the simulations show the same qualitative behavior, namely that κ falls strongly and nonlinearly with increasing porosity.

The high value of the exponent, $n = 4.70$, indicates that the staggered zigzag pore-wall architecture is an extremely efficient method for reducing κ. From the point of view of design, this means that rather than attempting to achieve high values of porosity, which can compromise mechanical properties, one can achieve comparable or even larger values of κ reduction at moderate values of porosity.

4 Conclusions

We presented a non-equilibrium molecular-dynamics study on heat transport in nanoporous silicon materials with a staggered, offset-pore ("zigzag") structure. The results demonstrate that thermal conductivity can be reduced by engineered pore structure much more significantly than by pore fraction alone.

The NEMD code was first verified by applying it to a size-scaling simulation on bulk silicon, where we varied lattice size over 13–104 nm, finding ballistic transport over this size range, and extrapolating to $\kappa_\infty \approx 148$ W/(m·K), as expected experimentally. In all comparisons between nanoporous and bulk materials, we have chosen to simulate at the same lattice size, $L_z = 26.1$ nm, so that size effects do not enter into the comparisons.

Two main observations emerge. First, introducing only 6.84% porosity in a single-pore geometry already lowers κ by 37%. Second, the staggered zigzag architecture at 28.27% porosity reduces κ by 78% — about twice the reduction suggested by effective-medium expectations at the same φ. Fitting $\kappa(\varphi)$ to $\kappa = \kappa_0(1 - \varphi)^n$ gives $n \approx 4.70$ (3.1× larger than the EMT reference $n = 1.5$). While this exponent is derived from two porosity values and should be considered indicative, it substantially exceeds the range reported for conventional pore geometries ($n \leq 3$), confirming the architecture-driven enhancement. Mechanistically, the enhancement follows from blocking direct pathways: offset pores force heat-carrying phonons through ~2.2 nm wall channels and impose two sharp turns, producing a compounded boundary-scattering penalty.

Overall, the results presented here validate the architecture-first approach for thermal metamaterial design, wherein optimization of pore location for intermediate porosities enables the design of structures with thermal performance exceeding those of higher porosity structures, with improved mechanical robustness. Future studies should (i) extend the porosities and motifs studied, (ii) extend the study to other semiconductor materials, such as GaN, and (iii) utilize the strong structure–property correlations observed here to train machine learning models for inverse design of thermal metamaterials [29].

Acknowledgment

This research was supported through computational resources of HPC-MARWAN (hpc.marwan.ma) provided by the National Center for Scientific and Technical Research (CNRST), Rabat, Morocco.

References

1. M. Maldovan, Sound and heat revolutions in phononics. Nature **503**, 209–217 (2013). https://doi.org/10.1038/nature12608
2. D.G. Cahill, P.V. Braun, G. Chen, D.R. Clarke, S. Fan, K.E. Goodson, P. Keblinski, W.P. King, G.D. Mahan, A. Majumdar, H.J. Maris, S.R. Phillpot, E. Pop, L. Shi, Nanoscale thermal transport. II. 2003–2012. Appl. Phys. Rev. **1**, 011305 (2014). https://doi.org/10.1063/1.4832615
3. J.-H. Lee, J.C. Grossman, J. Reed, G. Galli, Lattice thermal conductivity of nanoporous Si: Molecular dynamics study. Appl. Phys. Lett. **91**, 223110 (2007). https://doi.org/10.1063/1.2817739
4. Y. He, D. Donadio, J.-H. Lee, J.C. Grossman, G. Galli, Thermal transport in nanoporous silicon: Interplay between disorder on mesoscopic and atomic scales. ACS Nano **5**, 1839–1844 (2011). https://doi.org/10.1021/nn2003184
5. J.-K. Yu, S. Mitrovic, D. Tham, J. Varghese, J.R. Heath, Reduction of thermal conductivity in phononic nanomesh structures. Nat. Nanotechnol. **5**, 718–721 (2010). https://doi.org/10.1038/nnano.2010.149
6. P.E. Hopkins, C.M. Reinke, M.F. Su, R.H. Olsson III, E.A. Shaner, Z.C. Leseman, J.R. Serrano, L.M. Phinney, I. El-Kady, Reduction in the thermal conductivity of single crystalline silicon by phononic crystal patterning. Nano Lett. **11**, 107–112 (2011). https://doi.org/10.1021/nl102918q
7. J. Fang, L. Pilon, Scaling laws for thermal conductivity of crystalline nanoporous silicon based on molecular dynamics simulations. J. Appl. Phys. **110**, 064305 (2011). https://doi.org/10.1063/1.3638054
8. L. de Sousa Oliveira, N. Neophytou, Large-scale molecular dynamics investigation of geometrical features in nanoporous Si. Phys. Rev. B **100**, 035409 (2019). https://doi.org/10.1103/PhysRevB.100.035409

9. L. de Sousa Oliveira, S.A. Hosseini, A. Greaney, N. Neophytou, Heat current anticorrelation effects leading to thermal conductivity reduction in nanoporous Si. Phys. Rev. B **102**, 205405 (2020). https://doi.org/10.1103/PhysRevB.102.205405
10. S.A. Hosseini, A. Davies, I. Dickey, N. Neophytou, P.A. Greaney, L. de Sousa Oliveira, Super-suppression of long phonon mean-free-paths in nano-engineered Si due to heat current anticorrelations. Mater. Today Phys. **27**, 100719 (2022). https://doi.org/10.1016/j.mtphys.2022.100719
11. P.A. Greaney, S.A. Hosseini, L. de Sousa Oliveira, A. Davies, N. Neophytou, Super-suppression of long-wavelength phonons in constricted nanoporous geometries. Nanomaterials **14**, 795 (2024). https://doi.org/10.3390/nano14090795
12. G. Romano, J.C. Grossman, Heat transfer in nanostructured materials predicted by phonon bulk mean free path distribution. J. Heat Transfer **137**, 071302 (2015). https://doi.org/10.1115/1.4029775
13. G. Romano, J.C. Grossman, Toward phonon-boundary engineering in nanoporous materials. Sci. Rep. **7**, 44379 (2017). https://doi.org/10.1038/srep44379
14. L. Yang, N. Yang, B. Li, Extreme low thermal conductivity in nanoscale 3D Si phononic crystal with spherical pores. Nano Lett. **14**, 1734–1738 (2014). https://doi.org/10.1021/nl403750s
15. H. de Araujo Oliveira, Z. Fan, A. Harju, L.F.C. Pereira, Tuning the thermal conductivity of silicon phononic crystals via defect motifs: Implications for thermoelectric devices and photovoltaics. ACS Appl. Nano Mater. **8**, 4364–4372 (2025). https://doi.org/10.1021/acsanm.4c01875
16. K.R. Hahn, C. Melis, L. Colombo, Thermal conduction and rectification phenomena in nanoporous silicon membranes. Phys. Chem. Chem. Phys. **24**, 13625–13632 (2022). https://doi.org/10.1039/D2CP00775D
17. F. Müller-Plathe, A simple nonequilibrium molecular dynamics method for calculating the thermal conductivity. J. Chem. Phys. **106**, 6082–6085 (1997). https://doi.org/10.1063/1.473271
18. A.P. Thompson, H.M. Aktulga, R. Berger, D.S. Bolintineanu, W.M. Brown, P.S. Crozier, P.J. in 't Veld, A. Kohlmeyer, S.G. Moore, T.D. Nguyen, R. Shan, M.J. Stevens, J. Tranchida, C. Trott, S.J. Plimpton, LAMMPS – a flexible simulation tool for particle-based materials modeling at the atomic, meso, and continuum scales. Comput. Phys. Commun. **271**, 108171 (2022). https://doi.org/10.1016/j.cpc.2021.108171
19. P.K. Schelling, S.R. Phillpot, P. Keblinski, Comparison of atomic-level simulation methods for computing thermal conductivity. Phys. Rev. B **65**, 144306 (2002). https://doi.org/10.1103/PhysRevB.65.144306
20. S.G. Volz, G. Chen, Molecular-dynamics simulation of thermal conductivity of silicon crystals. Phys. Rev. B **61**, 2651–2656 (2000). https://doi.org/10.1103/PhysRevB.61.2651
21. D.P. Sellan, E.S. Landry, J.E. Turney, A.J.H. McGaughey, C.H. Amon, Size effects in molecular dynamics thermal conductivity predictions. Phys. Rev. B **81**, 214305 (2010). https://doi.org/10.1103/PhysRevB.81.214305
22. K. Esfarjani, G. Chen, H.T. Stokes, Heat transport in silicon from first-principles calculations. Phys. Rev. B **84**, 085204 (2011). https://doi.org/10.1103/PhysRevB.84.085204

23. C.J. Glassbrenner, G.A. Slack, Thermal conductivity of silicon and germanium from 3°K to the melting point. Phys. Rev. **134**, A1058–A1069 (1964). https://doi.org/10.1103/PhysRev.134.A1058
24. C.-W. Nan, R. Birringer, D.R. Clarke, H. Gleiter, Effective thermal conductivity of particulate composites with interfacial thermal resistance. J. Appl. Phys. **81**, 6692–6699 (1997). https://doi.org/10.1063/1.365209
25. N.K. Ravichandran, A.J. Minnich, Coherent and incoherent thermal transport in nanomeshes. Phys. Rev. B **89**, 205432 (2014). https://doi.org/10.1103/PhysRevB.89.205432
26. R. Dettori, C. Melis, X. Cartoixà, R. Rurali, L. Colombo, Model for thermal conductivity in nanoporous silicon from atomistic simulations. Phys. Rev. B **91**, 054305 (2015). https://doi.org/10.1103/PhysRevB.91.054305
27. G. Gesele, J. Linsmeier, V. Drach, J. Fricke, R. Arens-Fischer, Temperature-dependent thermal conductivity of porous silicon. J. Phys. D: Appl. Phys. **30**, 2911–2916 (1997). https://doi.org/10.1088/0022-3727/30/21/001
28. K. Zhu, J. Wang, C. Xu, G. Cheng, R. Zheng, Abnormal anisotropic thermal conductivity in porous silicon membranes. Int. J. Heat Mass Transfer **241**, 126743 (2025). https://doi.org/10.1016/j.ijheatmasstransfer.2025.126743
29. C. Zhu, E.A. Bamidele, X. Shen, G. Zhu, B. Li, Machine learning aided design and optimization of thermal metamaterials. Chem. Rev. **124**, 4258–4331 (2024). https://doi.org/10.1021/acs.chemrev.3c00708